Three-dimensional nano-localization of single fluorescent emitters

Iwan Märki, Noelia L. Bocchio, Stefan Geissbuehler, François Aguet, Alberto Bilenca and Theo Lasser

Ecole Polytechnique Fédérale de Lausanne, CH-1015, Lausanne, Switzerland

iwan.maerki@epfl.ch

Abstract: We present a combination of self-interference microscopy with lateral super-resolution microscopy and introduce a novel approach for localizing a single nano-emitter to within a few nanometers in all three dimensions over a large axial range. We demonstrate nanometer displacements of quantum dots placed on top of polymer bilayers that undergo swelling when changing from an air to a water environment, achieving standard deviations below 10 nm for axial and lateral localization.

OCIS codes: (180.0180) Microscopy; (180.2520) Fluorescence microscopy; (300.6280) Spectroscopy, fluorescence and luminescence.

References and links

1. G. Donnert, J. Keller, R. Medda, M. A. Andrei, S. O. Rizzoli, R. Lührmann, R. Jahn, C. Eggeling, and S. W. Hell, "Macromolecular-scale resolution in biological fluorescence microscopy," Proc. Natl. Acad. Sci. USA **103**, 11440–11445 (2006).
2. B. Hein, K. I. Willig, and S. W. Hell, "Stimulated emission depletion (sted) nanoscopy of a fluorescent protein-labeled organelle inside a living cell," Proc. Natl. Acad. Sci. USA **105**, 14271–14276 (2008).
3. R. Schmidt, C. A. Wurm, S. Jakobs, J. Engelhardt, A. Egner, and S. W. Hell, "Spherical nanosized focal spot unravels the interior of cells," Nat. Methods **5**, 539–544 (2008).
4. V. Westphal, S. O. Rizzoli, M. A. Lauterbach, D. Kamin, R. Jahn, and S. W. Hell, "Video-rate far-field optical nanoscopy dissects synaptic vesicle movement," Science **320**, 246–249 (2008).
5. E. Betzig, G. H. Patterson, R. Sougrat, O. W. Lindwasser, S. Olenych, J. S. Bonifacino, M. W. Davidson, J. Lippincott-Schwartz, and H. F. Hess, "Imaging intracellular fluorescent proteins at nanometer resolution," Science **313**, 1642–1645 (2006).
6. B. Huang, S. Jones, B. Brandenburg, and X. Zhuang, "Whole-cell 3D storm reveals interactions between cellular structures with nanometer-scale resolution," Nat. Methods **5**, 1047–1052 (2008).
7. J. S. Biteen, M. A. Thompson, N. K. Tselentis, G. R. Bowman, L. Shapiro, and W. E. Moerner, "Super-resolution imaging in live caulobacter crescentus cells using photoswitchable eyfp," Nat. Methods **5**, 947–949 (2008).
8. J. Vogelsang, T. Cordes, C. Forthmann, C. Steinhauer, and P. Tinnefeld, "Controlling the fluorescence of ordinary oxazine dyes for single-molecule switching and superresolution microscopy," Proc. Natl. Acad. Sci. USA **106**, 8107–8112 (2009).
9. B. Huang, W. Wang, M. Bates, and X. Zhuang, "Three-dimensional super- resolution imaging by stochastic optical reconstruction microscopy," Science **319**, 810–813 (2008).
10. S. R. P. Pavani, M. A. Thompson, J. S. Biteen, S. J. Lord, N. Liu, R. J. Twieg, R. Piestun, and W. E. Moerner, "Three-dimensional, single-molecule fluorescence imaging beyond the diffraction limit by using a double-helix point spread function," Appl. Phys. Lett **106**, 2995–2999 (2009).
11. P. V. Ganesan and S. G. Boxer, "A membrane interferometer," Proc. Natl. Acad. Sci. USA **106**, 5627–5632 (2009).
12. L. Moiseev, M. S. Unlü, A. K. Swan, B. B. Goldberg, and C. R. Cantor, "Dna conformation on surfaces measured by fluorescence self-interference," Proc. Natl. Acad. Sci. USA **103**, 2623–2628 (2006).
13. G. Shtengel, J. Galbraith, C. Galbraith, J. Lippincott-Schwartz, J. Gillette, S. Manley, R. Sougrat, C. Waterman, P. Kanchanawong, M. Davidson, R. Fetter, and H. Hess, "Interferometric fluorescent super-resolution microscopy resolves 3D cellular ultrastructure," Proc. Natl. Acad. Sci. USA **106**, 3125–3130 (2009).

#130650 - $15.00 USD Received 29 Jun 2010; revised 1 Sep 2010; accepted 2 Sep 2010; published 8 Sep 2010

14. A. Swan, L. Moiseev, C. Cantor, and B. Davis, "Toward nanometer-scale resolution in fluorescence microscopy using spectral self-interference," IEEE J. Sel. Top. Quantum Electron. **9**, 294–300 (2003).
15. F. Aguet, S. Geissbuehler, I. Maerki, T. Lasser, and M. Unser, "Super-resolution orientation estimation and localization of fluorescent dipoles using 3-D steerable filters," Opt. Express **17**, 6829–6848 (2009).
16. G. Decher, "Fuzzy nanoassemblies: toward layered polymeric multicomposites," Science **277**, 1232–1237 (1997).
17. L. Moiseev, C. Cantor, M. Aksun, M. Dogan, B. Goldberg, A. Swan, and M. Unlu, "Spectral self-interference fluorescence microscopy," J. Appl. Phys. **96**, 5311–5315 (2004).
18. M. Born and E. Wolf, *Principles of Optics: Electromagnetic Theory of Propagation, Interference and Diffraction of Light* (7th ed.) (Cambridge University Press, 1999).
19. S. Gibson and F. Lanni, "Experimental test of an analytical model of aberration in an oil-immersion objective lens used in 3-dimensional light-microscopy," J. Opt. Soc. Am. A **8**, 1601–1613 (1991).
20. M. K. Cheezum, W. F. Walker, and W. H. Guilford, "Quantitative comparison of algorithms for tracking single fluorescent particles," Biophys. J. **81**, 2378–2388 (2001).
21. D. Patra, I. Gregor, J. Enderlein, and M. Sauer, "Defocused imaging of quantum-dot angular distribution of radiation," Appl. Phys. Lett. **87**, 101103 (2005).
22. B. Richards and E. Wolf, "Electromagnetic diffraction in optical systems. 2. Structure of the image field in an aplanatic system," Proc. R. Soc. London, Ser. A **253**, 358–379 (1959).
23. M. Dogan, A. Yalcin, S. Jain, M. B. Goldberg, A. K. Swan, M. S. Unlu, and B. B. Goldberg, "Spectral self-interference fluorescence microscopy for subcellular imaging," IEEE J. Sel. Top. Quantum Electron. **14**, 217–225 (2008).
24. A. Swan, L. Moiseev, C. Cantor, B. Davis, S. Ippolito, W. Karl, B. Goldberg, and M. Unlu, "Toward nanometer-scale resolution in fluorescence microscopy using spectral self-interference," IEEE J. Sel. Top. Quantum Electron. **9**, 294–300 (2003).
25. A. Bilenca, A. Ozcan, B. Bouma, and G. Tearney, "Fluorescence coherence tomography," Opt. Express **14**, 7134–7143 (2006).
26. W. Barnes, "Fluorescence near interfaces: the role of photonic mode density," J. Mod. Opt. **45**, 661–699 (1998).
27. J. Antelman, C. Wilking-Chang, S. Weiss, and X. Michalet, "Nanometer distance measurements between multicolor quantum dots," Nano Lett. **9**, 2199–2205 (2009).
28. B. J. Davis, A. K. Swan, M. S. Unlü, W. C. Karl, B. B. Goldberg, J. C. Schotland, and P. S. Carney, "Spectral self-interference microscopy for low-signal nanoscale axial imaging," J. Opt. Soc. Am. A **24**, 3587–3599 (2007).
29. G. Decher and J. Schmitt, "Fine-tuning of the film thickness of ultrathin multilayer films composed of consecutively alternating layers of anionic and cationic polyelectrolytes," Prog. Colloid Polym. Sci. **89**, 160–164 (1992).
30. K. Vasilev, W. Knoll, and M. Kreiter, "Fluorescence intensities of chromophores in front of a thin metal film," J. Chem. Phys. **120**, 3439–3445 (2004).
31. K. Vasilev, F. Stefani, V. Jacobsen, W. Knoll, and M. Kreiter, "Reduced photobleaching of chromophores close to a metal surface," J. Chem. Phys. **120**, 6701–6704 (2004).
32. N. L. Bocchio, A. Unger, M. Alvarez, and M. Kreiter, "Thin layer sensing with multipolar plasmonic resonances," J. Phys. Chem. C **112**, 14355–14359 (2008).
33. A. Yalçin, F. Damin, E. Ozkumur, G. di Carlo, B. B. Goldberg, M. Chiari, and M. S. Unlü, "Direct observation of conformation of a polymeric coating with implications in microarray applications," Anal. Chem. **81**, 625–630 (2009).

1. Introduction

Using intrinsic fluorescence properties, super-resolution techniques such as STED microscopy [1, 2, 3, 4] and localization microscopy (PALM, STORM) [5, 6, 7, 8] have enabled the observation of subcellular structures at unprecedented details. Typically, these nanoscopy approaches have been focused on the manipulation and detection of the intensity of fluorescence light leading to a lateral accuracy of a few nanometers. However, three-dimensional nanometer-scale accuracy, in particular along the optical axis, remains a challenge. The axial localization accuracy can be improved to a few tens of nanometers by introducing optical astigmatism [9], by using helical wavefronts [10] or engineered excitation patterns [3], without substantially affecting the lateral accuracy. Alternatively, measuring the phase of fluorescence light has been shown to be valuable for axial measurements at the nano-scale. For example, in fluorescence interference contrast microscopy (FLIC), the change in the total emission intensity is a function of the distance from a nearby reflecting surface [11]. The axial information is extracted from the intensity in reference to a calibration of the position. A related technique is spectral self-

#130650 - $15.00 USD Received 29 Jun 2010; revised 1 Sep 2010; accepted 2 Sep 2010; published 8 Sep 2010

interference fluorescence microscopy (SSFM) where the spectral signature of the fluorescent emitters placed above a reflecting surface is used to determine the axial position with an accuracy of a few nanometers [12]. Until now none of these approaches, which consider the phase of the fluorescence emission, have been applied to single molecule measurements. Only recently, a first interferometric localization microscopy technique, called interferometric photoactivated localization microscopy (iPALM), has shown three-dimensional localization resolution below 20 nm [13, 14]. This technique combines PALM with single-photon multiphase interferometry based on a 4π configuration, a 3-way beamsplitter and three phase-shifted area detectors, in a classical concept similar to low coherence or phase shifting interferometry. However, without depth scanning, the axial range is limited by the three interference images to less than the central wavelength of the emission.

Here, we present a combination of self-interference microscopy at the single-emitter level with lateral super resolution microscopy and demonstrate a novel approach for localizing a single nano-object to within a few nanometers in all three dimensions. For lateral localization, we consider the complex emission pattern of a single fluorescent emitter, which not only yields an improved estimation of the axial position but also an improved lateral accuracy, as well as information on the orientation of the fluorescent emitter [15]. As a proof of principle, we demonstrate the measurement of nanometer displacements of quantum dots placed on polymer bilayers that undergo swelling when changing from an air to a water environment [16]. We expect that this technique will open up new possibilities for biological investigations with three-dimensional molecular resolution.

2. Experimental Setup

As illustrated in Figure 1(a), the experimental arrangement provides three-dimensional localization information for single quantum-dots, due to the parallel detection configuration based on both imaging and spectroscopy. The fluorescence image allows us to precisely localize the single quantum-dot in the lateral dimension, whereas the interference spectrum offers the precise localization of the quantum-dot in the axial direction similar to spectral self-interference fluorescence microscopy [17].

Nano-emitters consisting of a single fluorescent quantum-dot (Qdot® 705 ITK^{TM} Streptavidin Conjugate from Invitrogen) are deposited on a layered, custom-made slide comprising a microscope glass coverslip, a dielectric mirror and silicon oxide (SiO_2) spacer layer with a thickness of 8 μm and a nanometer-thick polymer layer (see Fig. 1(b)). The dielectric mirror is fabricated by alternating deposition of silicon nitride and silicon oxide layers onto the glass coverslip by means of plasma enhanced chemical vapor deposition (PECVD). The substrate was designed such as to efficiently transmit the excitation light as well as to reflect the emission of the fluorescent quantum-dot.

Figure 1(c) depicts the reflection properties of this dielectric mirror. In the wavelength range of the fluorescence emission, the dielectric mirror reflects the light incident with small angles. For incident angles higher than 50 degrees the emitted light from the quantum-dot is partially transmitted through the mirror. The fluorescent quantum-dot is excited in a widefield or TIRF configuration and imaged by a high NA (Zeiss Fluar 100x, NA=1.45) oil immersion objective onto an EMCCD camera (Andor Luca DL 658M EMCCD). Due to the dielectric mirror, the image results in a characteristic ring-shaped diffraction pattern. In addition, a low numerical aperture objective (NA=0.12) is placed above the sample to collect the spectral interference signal cast by the forward-directed and back-reflected fluorescence fields, as illustrated in Figure 1(a) and (b). The interference signal is then coupled to the spectrometer. A grating of 1800 grooves per millimeter provides a spectral resolution of 0.15 nm at a central wavelength of 700 nm. The spectral signal is recorded by a cooled charge coupled device (Andor DV434

#130650 - $15.00 USD Received 29 Jun 2010; revised 1 Sep 2010; accepted 2 Sep 2010; published 8 Sep 2010

CCD Camera) with an integration time of a few seconds to a minute depending on the spectral resolution and the NA of the collection objective.

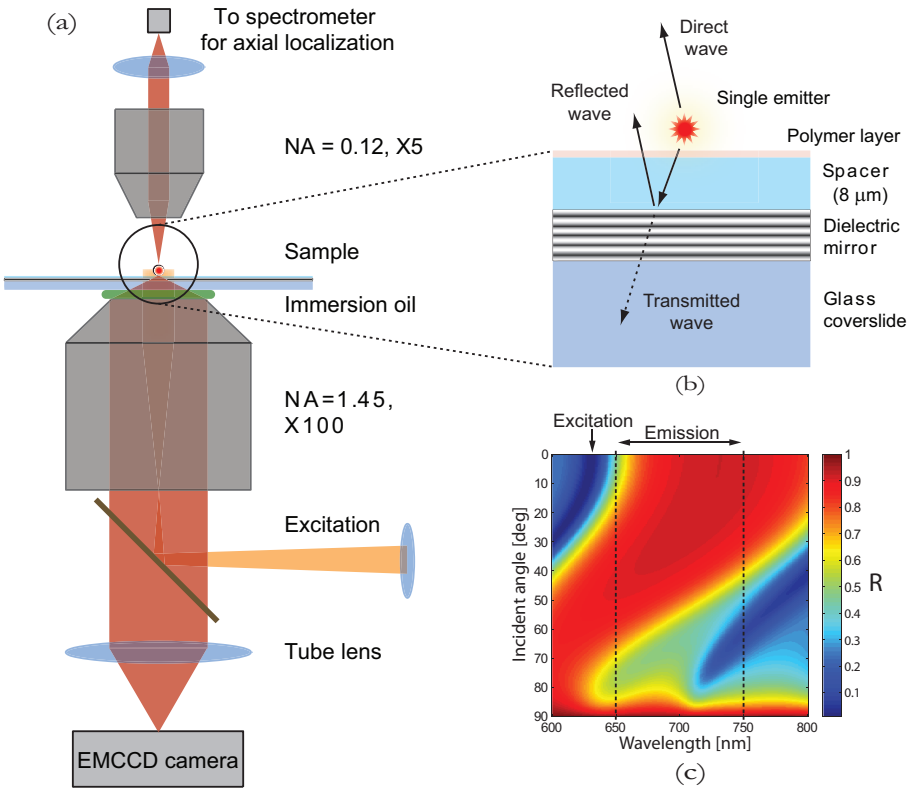

Fig. 1. (a) Experimental setup for three-dimensional localization of single fluorescent nano-objects. (b) Detail illustration of a quantum dot on the custom-made slide comprising the dielectric mirror and spacer layer. (c) Reflection properties of the dielectric mirror.

3. Lateral localization

Lateral localization of the fluorescent particle is achieved by fitting a vectorial point spread function (PSF) model to the intensity pattern recorded by the CCD. To this end, we extend a PSF model for fluorescent dipoles (see Ref. [15] and references therein) to incorporate the effects of the dielectric mirror in our system. This extension involves the adjustment of both the Fresnel coefficients for the mirror and the phase term in the PSF. The former are calculated through the appropriate characteristic matrices [18]. The phase term in the PSF corresponds to the optical path difference (OPD) between ideal imaging conditions for a point source located at the coverslip/sample interface and actual acquisition settings [19]. Consequently, the correct phase terms are integrated in a generalization of the Gibson and Lanni model [19], which takes into account for the additional optical path difference introduced by the mirror.

Frequently, lateral localization is performed by fitting a 2-D Gaussian to the image of individual fluorophores. While this leads to high localization accuracies for sources that are within the focal plane [20], the accuracy decreases for out-of-focus fluorophores, whose images present complex, ring-shaped patterns. Here, the ring-shaped diffraction patterns are amplified by the dichroic mirror. Figure 2 presents an experimentally measured (a) and fitted (b) diffraction pat-

#130650 - $15.00 USD Received 29 Jun 2010; revised 1 Sep 2010; accepted 2 Sep 2010; published 8 Sep 2010

tern for an in-focus quantum dot. The physically realistic image formation model is thus used to maximize the localization accuracy.

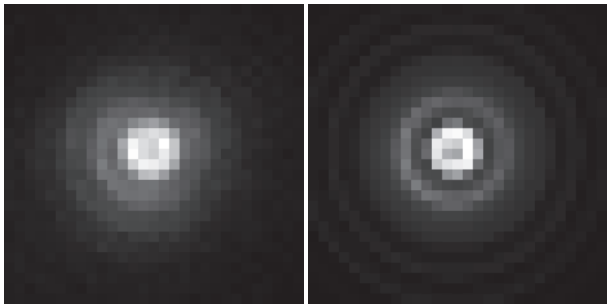

(a) (b)

Fig. 2. (a) Measured diffraction pattern of a single quantum dot. (b) Fitted diffraction pattern for precise lateral localization based on the realistic image formation model.

The emission pattern of a quantum dot can be expressed as a superposition of three orthogonal dipoles with different radiation weights [21]. In our implementation, we used an extended 3-D steerable dipole model by incorporating three Euler angles for the orientation (φ, ψ, ω) as well as two additional weighting factors (κ, η) accounting for the degeneracy of the dipole emission (Eq. (1-7)). The basic approach is described by Aguet et al. [15].

$$h_{\varphi,\psi,\omega,\kappa,\eta}(\mathbf{x};\mathbf{x}_p,\tau) = \mathbf{c}^T(\varphi,\psi,\omega,\kappa,\eta)\cdot\mathbf{m}(\mathbf{x};\mathbf{x}_p,\tau) \tag{1}$$

$\mathbf{m}$ is a vector that contains six non-orthogonal basis templates depending on the observation point $\mathbf{x} = (-r\cos\psi_d, -r\sin\psi_d, z) = (\sqrt{(x-x_p)^2+(y-y_p)^2}, tan^{-1}((y-y_p)/(x-x_p)), z)$, the position of the particle in the sample space $\mathbf{x}_p = (x_p, y_p, z_p)$ and the optical parameters of the setup τ. It is given by

$$\begin{aligned}
m_1 &= |I_0|^2 + |I_2|^2 && (2)\\
m_2 &= \sin(2\psi_d)\mathfrak{Re}\{I_0^* I_2\} && (3)\\
m_3 &= \cos(2\psi_d)\mathfrak{Re}\{I_0^* I_2\} && (4)\\
m_4 &= \sin(\psi_d)\mathfrak{Im}\{I_1^*(I_0+I_2)\} && (5)\\
m_5 &= \cos(\psi_d)\mathfrak{Im}\{I_1^*(I_0+I_2)\} && (6)\\
m_6 &= |I_1|^2 && (7)
\end{aligned}$$

where $I_{0/1/2}(r,z,z_p,\tau)$ are the Richards-Wolf integrals [22]. $\mathbf{c}$ consists of trigonometric interpolation functions according to the orientation of the triple dipole (φ,ψ,ω) and accounts for the weighting factors κ and η. The fit was performed using a least-squares based minimization (see 2(b)). Using this approach, we achieved a lateral localization accuracy below 10 nm (see results).

4. Axial localization

The localization of the fluorescent emitter in the axial dimension is based on spectral self-interference fluorescence microscopy [17, 23]. Fluorescence self-interference has been used to determine axial dimensions and displacements of fluorescent molecules above reflecting layers at the nanometer scale, by measuring the intensity as well as spectral phase shifts [24].

#130650 - $15.00 USD Received 29 Jun 2010; revised 1 Sep 2010; accepted 2 Sep 2010; published 8 Sep 2010

Techniques such as fluorescence coherence tomography [25] are based on intensity information for measurements in the micrometer range, where as spectral self-interference fluorescence microscopy is based on the phase information for measurements in the nanometer range.

An emitter situated above the silicon oxide spacer layer and the reflecting dielectric mirror exhibits modified spontaneous emission rates due to the interaction with the interface [26]. The interference between the forward-directed and the back-reflected emission fields induces spectral oscillations within the spectral envelope of the fluorescent emitter (see Fig. 1 and Fig. 3). A long path length difference between direct and reflected light, i.e., a spacer thickness of several times the coherence length of the fluorescence light, means that only a small change in the wavelength is needed to cause constructive and destructive interference, thus increasing the number of interference oscillations. These oscillations encode the axial position information of the fluorescent emitter. Periodicity and phase of the oscillations change as a function of axial position. The axial and lateral resolutions are decoupled, whereas the axial resolution depends on the number of spectral oscillations and the resolution of the spectrometer. In order to reconstruct the axial position of the fluorescent object from a measured spectrum, an accurate physical model of the experimental self-interference configuration is necessary [17].

The fluorescent nano-object is generally modeled as a dipole emitter with a random orientation. Quantum dots, as used in our experiment, exhibit radiation characteristics of elliptically degenerate dipole emitters due to their non-spherical shapes [21]. In particular, it has been shown that quantum dots emitting in the longer wavelength range (600 to 700 nm) have a slightly elliptical shape, which enforces a more or less pronounced dipole emission pattern [27].

Considering only the far-field expressions of the emitted waves, as suggested by Moiseev et al. [17], the resulting interference components of the intensity for a single emitter is given by

$$I = |E_{TE,TM}(\theta,\varphi,\psi) + E_{TE,TM}(\pi-\theta,\varphi,\psi)R_{TE,TM}(n,D,\lambda,\theta)e^{ik2d\cos\theta}|^2. \quad (8)$$

The electric field components $E_{TE,TM}$ emitted by the dipole depend on θ, the emission or collection angle, and on φ and ψ, the polar and azimuthal orientation angles of the dipole, respectively. The silicon oxide spacer layer is characterized by its thickness D and its refractive index n, whereas d describes the height position of the fluorescent emitter above the surface. The back-reflected field is modified by the reflection coefficients of the dielectric mirror. The wavelength-dependent coefficients are calculated by means of the characteristic matrix describing the periodic multilayer with the corresponding refractive indices and layer thicknesses [18].

The total intensity collected by the objective is then calculated by integrating the emission over the collection angle, defined by the numerical aperture of the objective ($NA = 0.12$). For a single fluorescent emitter, the unknown parameters that have to be fitted to the measured spectrum are d, the axial position, and ψ, the polar orientation of the dipole. In our case, where quantum dots are used as fluorescent emitters, the dipole characteristic is degenerated [21]. Therefore, we integrate over several polar dipole orientations including slight errors well below the localization accuracy and simplify the fitting to only one parameter, the axial position d.

As a first step, the envelope of the spectrum is retrieved by Fourier filtering the oscillatory components of the measured spectral self-interference signal (see inset in Figure 3(a)). The obtained envelope of the spectrum serves as the emission profile of the fluorescent emitter in the scalar model, which includes the experimental and sample parameters such as the numerical aperture of the collection objective and the spacer layer thickness. As a next step, the measured data is used to find a solution based on the scalar model that is close to the unknown parameter, i.e., the axial position of the quantum dot. Davis et al. have investigated several ways of performing this estimation, such as maximum likelihood estimation and Richardson-Lucy reconstruction [28]. In this proof of principle we apply least-squares non-linear curve fitting by

#130650 - $15.00 USD Received 29 Jun 2010; revised 1 Sep 2010; accepted 2 Sep 2010; published 8 Sep 2010

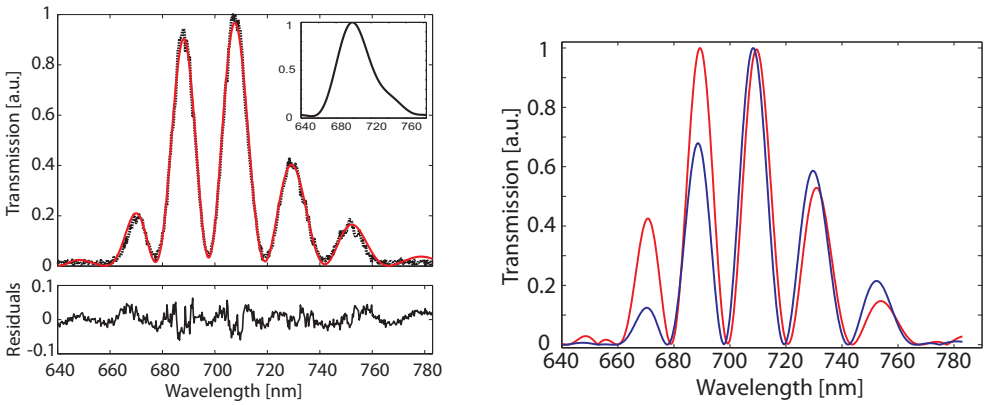

(a) (b)

Fig. 3. (a) Experimental spectral self-interference signal of a single quantum dot (blue), and the corresponding fit by least-squares non-linear curve fitting (red). The inset represents the envelope of the spectrum retrieved by Fourier filtering of the oscillatory components. Differences between the fit and the measured data shown in the residuals are due to aberrations in the spectrometer and the present noise. (b) Fitted measurements (red and blue) of two quantum dots differing in their axial position by 20 nm.

computing the scalar model, justified by the low NA, with the axial position parameter that fits best the measured spectral self-interference signal. As shown in Figure 3(a), this localization algorithm leads to a good fit to the experimental data. Figure 3(b) presents two fitted measurements from two quantum dots that differ in their axial position by 20 nm, demonstrating the small spectral phase shift corresponding to the difference in axial position.

The robustness of the fitting process depends on the signal-to-noise ratio (SNR) of the measured signal and the accuracy of the fixed experimental and sample parameters. Autofluorescence caused by impurities at the interfaces between silicon nitride and silicon oxide layers contributes to a background containing self-interference oscillatory components, which perturb the signal from the single emitting particle and decrease the signal to noise ratio. Therefore, the spectral measurements are background corrected, eliminating most of the perturbation due to autofluorescence. The axial range, where the position of a particle can be determined, is physically limited by the spectral resolution of the spectrometer and the numerical aperture of the collection objective. Simulations of self-interference signals with a SNR ($SNR_{measured}$=20), closely mimicking the experimental configuration, yielded an axial range of up to 100 μm with a localization precision of a few nanometers. Figure 4(a) shows the fitting performance on the modeled self-interference signals (SNR=20) in terms of the average accuracy of the axial localization over the whole axial range. Experimentally, this was confirmed by measuring a 50 μm thick polymer film. The corresponding spectral self-interference signal is shown in Fig. 4(b). Recent high-resolution microscopy methods [10, 3, 13] exhibit limited axial localization of a few hundreds of nanometers. Fluorescence self-interference microscopy, though, offers an axial range of ten's of micrometers, the typical thickness of cells. This great axial range and nanometer accuracy stems from the fact that not only the periodicity but also the phase of the spectral oscillation depend on the axial position of the emitter. When two or more particles with different axial positions are measured simultaneously, their spectral signature overlap. For such a configuration, the scalar model can be adapted. However, the reconstruction becomes more complex [28].

#130650 - $15.00 USD Received 29 Jun 2010; revised 1 Sep 2010; accepted 2 Sep 2010; published 8 Sep 2010

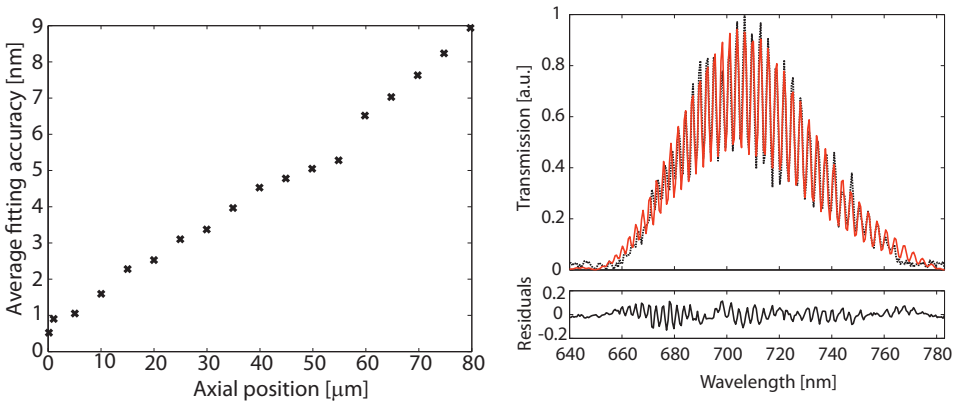

(a) (b)

Fig. 4. (a) Average accuracy of the axial localization fitting process on ten modeled self-interference signals (SNR=20) over the axial range of several ten's of micrometers. (b) Measured spectral self-interference signal (dashed black) with the corresponding fit (red) of a quantum dot on a thick polymer film yielding a thickness of 48.683 μm. Differences between the fit and the measured data shown in the residuals are due to aberrations in the spectrometer and the present noise. In particular, it is visible at the sides of the spectrum, where aberrations are stronger and the signal smaller.

5. Sample preparation

In order to demonstrate the validity of our three-dimensional nano-localization approach, we observe the characteristic vertical displacement of the nanometer-thick polymer bilayers when exposing the substrate to a water environment. Polyelectrolyte multi-layers were deposited onto the silicon oxide spacer layer using polyallylamine (PAH) and polystyrene sulfonate (PSS) as polycation and polyanion, respectively [16, 29]. Polyallylamine hydrochloride (PAH) (Aldrich, Mw = 15000) and polystyrene sulfonate (PSS) (Aldrich, Mw = 70000) aqueous solutions were prepared for this purpose. A water solution of PSS was dialysed during 3 days (Spectra Por 6, MWCO: 30000) prior to its use; the PAH was used as received from the manufacturer. The solutions were brought to pH 3 via adding HCl. Salts were added to adjust the ionic strength of the solutions [16, 29]. The concentration of the polyelectrolytes was 0.02 M (in monomer units), 0.5 M for the $MnCl_2$ (PSS solution) and 2 M for NaBr (in the PAH solution) [30, 31, 32]. After functionalizing the SiO_x layer with an amino-terminated silane (3-aminopropyltri-etoxy silane, Altrich 3-APTES), the substrates were exposed sequentially to the PSS (-) and PAH (+) solutions to build up the bilayers (1 bilayer = 1 PSS layer + 1 PAH layer). For each bilayer cycle, a drop of PSS was placed on the substrate for 20 min, rinsed several times with distilled water and dried. After this, exactly the same procedure was repeated using the PAH solution, finally building up a bilayer. The process can be repeated as many times as necessary in order to obtain a given thickness. In this experiment, we built a 6-bilayer and a 10-bilayer substrate with a thickness of 40 nm and 70 nm, respectively. A 2 nM solution of quantum dots (QDs), made from a dilution of an original stock of 1 μM Qdot 705 Streptavidin Conjugate QDs, was deposited on the substrates (PAH terminated layers) for a few minutes, rinsed with water and blown dry.

#130650 - $15.00 USD Received 29 Jun 2010; revised 1 Sep 2010; accepted 2 Sep 2010; published 8 Sep 2010

6. Results and Discussion

Due to the presence of water the polyelectrolyte multi-layers slightly swell and consequently the thickness increases. The swelling depends on the number of multi-layers, on the properties of the polymer, as well as the environmental conditions [16]. According to surface plasmon resonance (SPR) measurements, the thickness for a 10-bilayer substrate increases by approximately 35 nm.

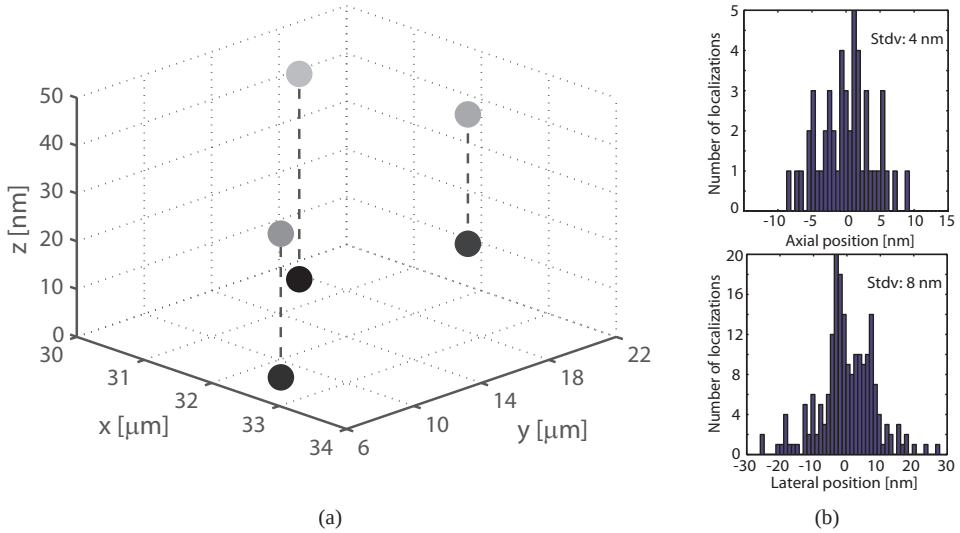

(a) (b)

Fig. 5. (a) Three-dimensional nano-localization. Single quantum dot localization measurements before (dark) and after swelling (light) of the polymer bilayers. The 10-bilayer substrate thickness increases by about 35 nm. (b) Histogram of 50 axial localizations yielding a standard deviation of 4 nm (upper graph) and histogram of 100 lateral localization yielding a standard deviation of 8 nm (lower graph).

Figure 5(a) depicts three measured quantum dots placed on the 10-bilayer substrate. We first measured the three-dimensional position of the three particles in an air environment. The lateral positions were imaged onto the EMCCD camera in the epi-illumination configuration (with an integration time of 0.3 seconds). The axial positions were obtained by sequentially exciting each of the single quantum dots and by recording the corresponding self-interference spectrum. In order to achieve this, we used a pinhole that limited the excitation field to a single quantum dot. Subsequently, the three-dimensional positions were determined by means of the lateral and axial localization fitting algorithms described above. Next, the same quantum dots were measured after adding a drop of water onto the polymer layers. Extracted from the combination of imaging and spectroscopy, Fig. 5(a) shows that, upon hydration of the bilayer substrates, the quantum dots undergo a vertical displacement of the order of 35 nm, matching estimations based on SPR measurements.

This confirms that our three-dimensional localization approach resolves the nanometer-scale displacements of the layers. Similar swelling observations of polymer layers based on average measurements of different DNA probes have shown a difference in the axial distribution of the probe molecules within the polymer structure [33]. Our approach, which allows for the observation of the three-dimensional position of individual particles, reveals a comparable variation in axial position (5 to 10 nm) between the measured quantum dots. Comparing the two states

#130650 - $15.00 USD Received 29 Jun 2010; revised 1 Sep 2010; accepted 2 Sep 2010; published 8 Sep 2010

of the polymer (non-swelled and swelled), we notice a lower variation between the quantum dots' axial positions when the polymer layers are in an air environment. We assume that certain surface and particle irregularities can give rise to slightly different heights upon the swelling of the polymer (see Figure 5(a)). In addition to the variation in axial position, the measurement precision is limited by the axial accuracy. To evaluate the experimental axial accuracy, we performed 50 measurements of the same single quantum dot with an integration time of 2 minutes. Following this, we applied the fitting process to each of the measurements. The obtained distribution of axial positions yielded a standard deviation of 4 nm as shown in the upper graph of Fig. 5(b). The lateral accuracy was calculated over 100 images and yielded a standard deviation of 8 nm (see lower graph of Fig. 5(b)). In addition, we calculated theoretical limits on axial localization accuracy by computing the Cramér-Rao lower bounds using a shot-noise limited noise model and respecting Nyquist's sampling theorem. For a defined exposure time this study showed an enhanced precision with increased pixel size and smaller emitter-to-mirror distances. In particular, for a localization precision of a few nanometers and an axial range of a few ten's of micrometers, as shown in this paper, integration times of a few seconds are needed allowing likewise the use of organic fluorophores as emitters.

A next step towards super-resolution microscopy consists in the detection of multiple particles within the same excitation field. Whereas for lateral localization concepts such as STORM, PALM and STED, are readily applicable, demultiplexing without a priori knowledge remains a great challenge for self-interference microscopy [28]. The reconstruction algorithms only work with the a priori knowledge that a few N emitters are constituting the spectral signal. However, in the case where the detection efficiency guarantees recording of the spectral signal within a second, we expect that the combination of STED and spectral self-interference microscopy will lead to simplified super-resolution fluorescence microscopy with nanometer resolution in all three dimensions over a large axial range.

7. Conclusion

We have demonstrated a new approach for three-dimensional localization of a single fluorescent nano-emitter. The combination of fluorescence imaging and self-interference microscopy allows us to simultaneously and precisely localize single quantum-dots within a few nanometers in both the lateral and axial dimension. Axial localization is based on fitting a scalar model of the measurement configuration to the measured self-interference spectrum of the single quantum dot, resulting in an axial localization accuracy with a standard deviation of the order of 4 nm. It has also proven valid for measurements in the micrometer range. Lateral localization is based on a theoretical diffraction model fitted to the characteristic emission of single quantum dot. The latter model, which takes into account the experimental configuration, such as the properties of the dielectric mirror and spacer layer, results in an improved lateral localization accuracy with a standard deviation of the order of 8 nm. Our work has confirmed nanometer accuracy in all three dimensions by measuring nanometer displacements of single quantum dots deposited on polymer bilayers that undergo swelling upon hydration. We believe that further development of this technique will open up new possibilities for investigations requiring three-dimensional molecular-resolution fluorescence imaging, such as topographic measurements of cellular structures or biophysical investigations on membrane functions.

8. Acknowledgments

We acknowledge N. Vogel for SPR measurements on the polyelectrolyte layers and we gratefully acknowledge the support from the European Commission and the Swiss national science foundation for the funding.

#130650 - $15.00 USD Received 29 Jun 2010; revised 1 Sep 2010; accepted 2 Sep 2010; published 8 Sep 2010